Surface Roughness of Mars

by

Andrew Benedict Mamo

Submitted to the Department of Physics
in partial fulfillment of the requirements for the degree of

Bachelor of Science in Physics

at the

MASSACHUSETTS INSTITUTE OF TECHNOLOGY

June 2004

Author .....
Department of Physics
May 7, 2004

Certified by .....
Maria T. Zuber
E. A. Griswold Professor of Geophysics
Thesis Supervisor

Accepted by .....
David E. Pritchard
Professor of Physics

Surface Roughness of Mars

by

Andrew Benedict Mamo

Submitted to the Department of Physics
on May 7, 2004, in partial fulfillment of the
requirements for the degree of
Bachelor of Science in Physics

Abstract

In this thesis, I created an algorithm to compensate for the saturation of data collected by the Mars Orbiter Laser Altimeter (MOLA). Saturation of the energy measurements had made it impossible to measure surface roughness at 100 m length scales. By calculating the returned energy, the problem of saturation can be avoided. This algorithm was applied to MOLA data across the Martian surface to create an estimate of surface roughness across the planet. The method calculates pulse spreading from returned pulse energy using the link equation. The accuracy of the method is limited by the accuracy of albedo measurements. This analysis improved the estimation of surface roughness on Mars. Further improvements could be gained by correcting for the opacity of atmospheric dust as a cause of pulse spreading.

Thesis Supervisor: Maria T. Zuber
Title: E. A. Griswold Professor of Geophysics

Acknowledgments

I would like to thank Prof. Maria Zuber for offering me the chance to work on this project. I would also like to thank Greg Neumann for providing advice throughout the year.

I am very grateful for the opportunity to become involved with the Mars community at such an exciting time for the field.

This work was supported by a generous grant from the John Reed UROP Fund.

Contents

List of Figures

Chapter 1

Introduction

There are few objects of scientific inquiry which combine great public interest with a wealth of truly important research opportunities to the degree that Mars does. The planet has occupied the public imagination ever since Percival Lowell described seeing canals on Mars in 1906 and posited the existence of intelligent Martian civilizations. Since then, Mars exploration has been a staple of science fiction. Only in the past half-century, however, has it been possible to explore Mars and to seriously consider sending humans there. In January, 2004, President Bush called for eventual manned missions to Mars. This announcement came on the heels of the successful landings of the Mars Exploration Rovers and the transmission of images taken from the Martian surface. These spacecraft were launched at a time when planetary orbits brought the Earth and Mars closer than they had been in years. The remarkable images that the rovers sent back offered the public a chance to get even closer to Mars.

Mars exploration has been a top priority of the scientific community for years. Its proximity to Earth makes it relatively accessible to spacecraft. It is tantalizingly similar to our own planet in many ways despite the obvious differences, making it a remarkable geological and climatological laboratory. Any efforts at understanding the formation of the solar system or at understanding the geological processes affecting our own planet must take Mars into account.

1.1 Overview of Mars Exploration

In 1965 Mariner 4 became the first spacecraft to travel to Mars. The first lander to survive the descent was the short-lived Mars 3 sent by the Soviet Union in 1971, which stopped transmitting data after 20 seconds. That same year Mariner 9 became the first spacecraft to orbit Mars, providing images of the entire Martian surface and the two moons Phobos and Deimos. These images revealed the expanse of the Valles Marineris canyon and the large volcanos around the Tharsis region, including the large Olympus Mons. The first maps of Mars were created using the data provided by Mariner 9. The year 1975 brought the launch of Viking 1 and 2, landing at Chryse Planitia (22°N, 310°E) and at Utopia Planitia (50°N, 135°E) respectively. These landers and their respective orbiters provided images of the Martian surface as well as important data on the planet's climate. These missions were very successful. Until recently the Viking data provided the bulk of our knowledge of Mars. Another important mission was the 1996 Pathfinder. This mission provided more images and more data on the Martian environment.

The Mars Global Surveyor (MGS) spacecraft was launched on November 7, 1996, by the Jet Propulsion Laboratory (JPL) and the National Aeronautics and Space Administration (NASA). Included on the spacecraft was the Mars Orbiter Laser Altimeter (MOLA) [1], an instrument designed to provide a detailed topographic map of the planet. This lidar measured over 600 million laser returns over two Martian years.

The laser transmitter consists of a Q-switched, chromium/neodymium-doped yttrium aluminum garnet (Cr:Nd:YAG) transmitter with aluminum gallium arsenide (AlGaAs) laser diodes. The laser operated at a wavelength of 1.064 μm and pulsed at 10 Hz with 8 ns full width at half maximum amplitude. In its 400 km orbit of MGS, MOLA measured height in a $\sim$ 150 m footprint on the Martian surface [2].

MOLA measured Martian topography by recording the round-trip time of flight of laser pulses. The reflected laser pulse echo was recorded within a certain range gate, over which the pulse exceeded a certain threshold. This gating mechanism

allowed for reliable measurement of pulses while reducing background noise and false measurements. The distance between the MGS spacecraft and the Martian surface can be found through the relation

$$Z_{Mars} = \frac{ct_{flight}}{2}. \tag{1.1}$$

where c is the speed of light and t_{flight} is the round-trip time of flight of individual laser pulses from the spacecraft to the Martian surface.

MOLA included four filters with different channel widths to receive measurements from different types of terrain. Returns from flat terrain were thus separated from returns from very strongly sloped surfaces, such as canyon walls, or returns from clouds. All data considered in this analysis was from the first channel, corresponding to the flattest terrain. This covers most of the Martian surface, and allows for a simple comparison between different methods. This channel corresponds to height variations within the footprint of 3 m, and footprint-scale slopes of 1° [1].

Measuring the surface roughness at the hundred meter length scale is important for a number of reasons. It is vital to know roughness for site selection for landers [3]. Landing delicate instrumentation on the Martian surface is difficult, and the problems magnify greatly in rough terrain. Of more immediate scientific interest, roughness data is essential for the project of understanding Martian geology and reconstructing that planet's history.

This paper considers the problem of measuring Mars surface roughness using the altimetric data taken by MOLA. The remainder of this section provides an overview of previous methods for determining surface roughness. The next section will describe the method used to provide an alternate assessment of surface roughness and will examine its limitations. In the third section, this method will be applied to the MOLA data to provide a new measurement of Martian surface roughness. The fourth section will reassess the prospects for accurate surface roughness measurement and will look beyond Mars to future lidar missions.

1.2 Overview of Surface Roughness Studies

Surface roughness measurements can be made along several different length scales. MOLA's design set the footprint size at $\sim$ 150 meters. Roughness measurements at length scales larger than the footprint work by measuring elevation differences between neighboring points. One analysis of kilometer-scale roughness [4] measured the slope between points 2.4 kilometers apart and the slope between points 4.8 kilometers apart. By subtracting the latter from the former, this analysis measures differential slopes while excluding the larger-scale tilting of the surface.

Measuring surface roughness at scales on the order of the footprint size calls for a different approach. The shape of the laser echo pulse reveals much about the topography of the region in the laser footprint. Different elevations within the region will reflect the light with different travel times, leading to pulse spreading. A height difference of h between two points would result in reflected photons returning with a time difference of $2h/c$, c being the speed of light. See fig. 1-1.

As shown in the fig. 1-1, pulse spreading can be caused by footprint roughness or by footprint-scale sloping. For much of the planet, the dominant cause of spreading is from roughness rather than slope [5].

Previous work [6] has already provided some good estimates of Martian surface roughness at hundred meter length scales. In places where the surface was bright and flat, so that the returned signal was strong, the signal strength exceeded the allowable range leading to a case of pulse saturation. However, the saturation of the MOLA data meant that these measurements were necessarily incomplete and could only take into account certain regions of the planet.

The approach used by Abshire et al. [7] calculates the root-mean-square pulse width σ from the photon count of the returned laser pulse echo. This method gives

$$\sigma = \frac{W_y}{2\sqrt{2}} \frac{1}{z^{-1}\left[\frac{A_y}{yW_y}\right]} \tag{1.2}$$

where W_y is the full pulse width at threshold, y is the threshold level, A_y is the pulse

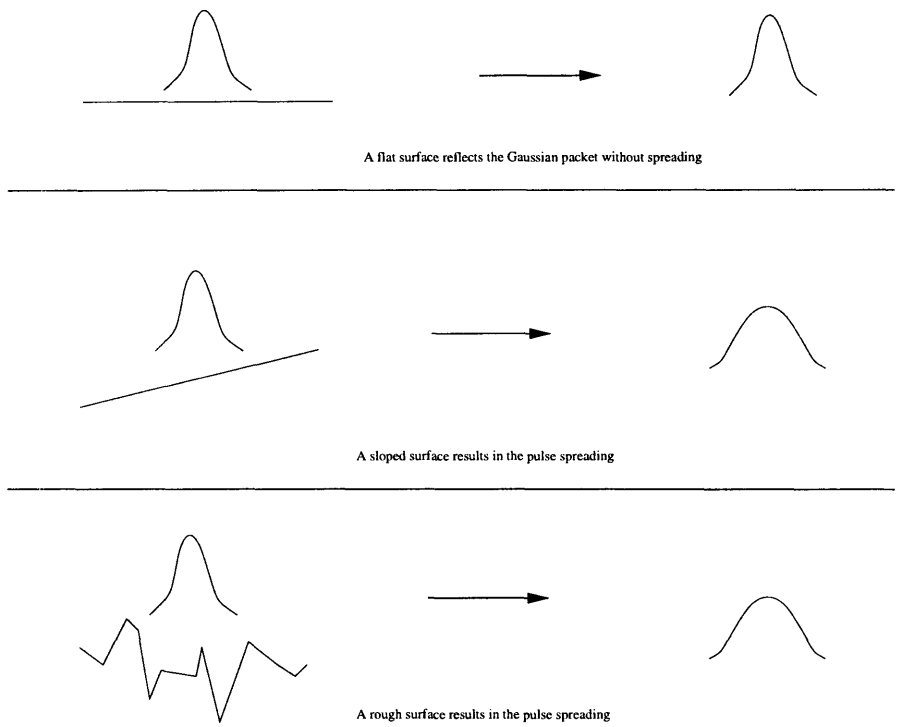

Figure 1-1: The effects of different surfaces on echo pulse spreading. Flat terrain leads to the pulse returning without spreading. Both sloped terrain and rough terrain cause spreading of the echo pulse.

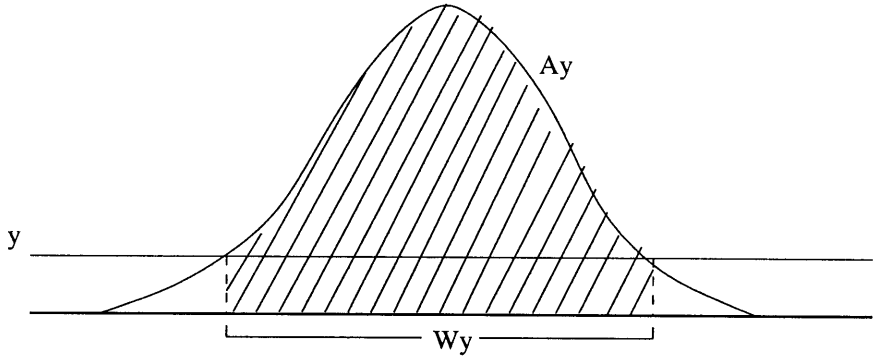

Figure 1-2: Pulse information from MOLA. y is the threshold level, W_y is the full width at threshold, and A_y is the integrated pulse area over W_y.

area integrated over W_y, and z^{-1} is the inverse of the function

$$\mathrm{z}(x) \equiv \frac{\sqrt{\pi}}{2} \frac{\mathrm{erf}(x)}{x \exp(-x^2)}.$$

The MOLA receiver recorded up to 255 photon counts. No higher energy values could be measured. Much of the Martian surface had a higher albedo than expected, making the total returned pulse energy larger than the saturation value. Therefore much of the surface could not be measured using this method. Furthermore, the inversion technique was sensitive to small measurement errors.

The echo pulse strength can be calculated from transmitted pulse energy and planetery properties through the laser link equation [7] described in the next chapter. The direct measurements of echo pulse energy used in the Abshire method are constrained by the instrumentation, whereas transmitted pulse energy is more easily known. Therefore, using the echo energy calculated by the link equation may prove to be more reliable than using the directly-measured energy, which is frequently saturated. Echo pulse energies calculated by the link equation are only as reliable as the parameters in the equation.

Surface roughness is related to the spreading of the Gaussian pulse. The Abshire method measures the spreading, σ, through equation 1.2. This method is not applicable when using the link equation. The method outlined in chapter 2 uses Taylor approximations to find σ from the calculated return energy, making it more robust

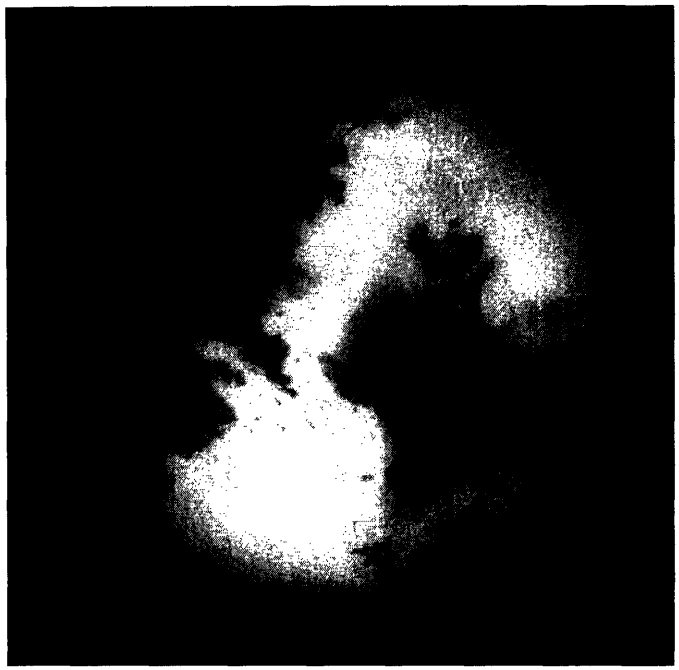

Figure 1-3: An image of Mars at 1.042 microns taken from Hubble Space Telescope, 27 April 1999.

and less dependent upon variation in albedo measurements.

1.3 Albedo Measurements

Three different measurements of albedo were used in this study. One such measurement was an active measurement by MOLA of reflected laser energy over transmitted energy. Another measurement was a passive radiometry measurement made after the MOLA laser stopped functioning, comparing received light to calculated incoming light at the 1.064 μm wavelength. These two methods both provided global coverage of Mars. The third method used measurements made by the Hubble Space Telescope (HST) rather than by MOLA [8]. Due to the tilt of Mars, the HST measurements do not provide global coverage.

While there is a general agreement among the different albedo measurements, this agreement is not perfect. The radiometry measurements were simply a ratio of incident light to solar flux (I/F), and they do not take the viewing geometry into

account.

Throughout this analysis, the inversion method used by Abshire will be compared against the method described in the next chapter. The inversion approach uses data on photon counts collected by MOLA, and it is therefore to be expected that calculations made with the MOLA-measured albedo will provide the best agreement with the previous calculations.

Chapter 2

Methodology

2.1 Evaluating Pulse Width σ

As mentioned in the introduction, the echo pulse energy for this work was calculated from the laser altimeter link equation [7]:

$$E_r = E_{tr}\tau_r \frac{A_r}{R_m^2}\frac{r_s}{\pi}\tau_a^2, \tag{2.1}$$

where E_r is the echo pulse energy, E_{tr} is the transmitted pulse energy, τ_r is the receiver optical transmission, A_r is the aperture area of the receiver telescope, R_m is the distance to the Martian surface, r_s is the surface reflectivity, and τ_a is the one-way atmospheric transmission. The echo pulse energy is related to the integrated echo area by

$$E_r = \frac{A}{R_{det}},$$

where R_{det} is the detector responsivity, measured to be $R_{det} = 1.26 \times 10^8$ V/W.

The pulse shape is approximately Gaussian:

$$V = \frac{A}{\sqrt{2\pi}\sigma} \exp\left[-\frac{1}{2}(t/\sigma)^2\right]. \tag{2.2}$$

MOLA measures the time over which the pulse exceeds a certain threshold of $V = .561$ nV. With V and A fixed, the width of the Gaussian can vary, which changes PWT,

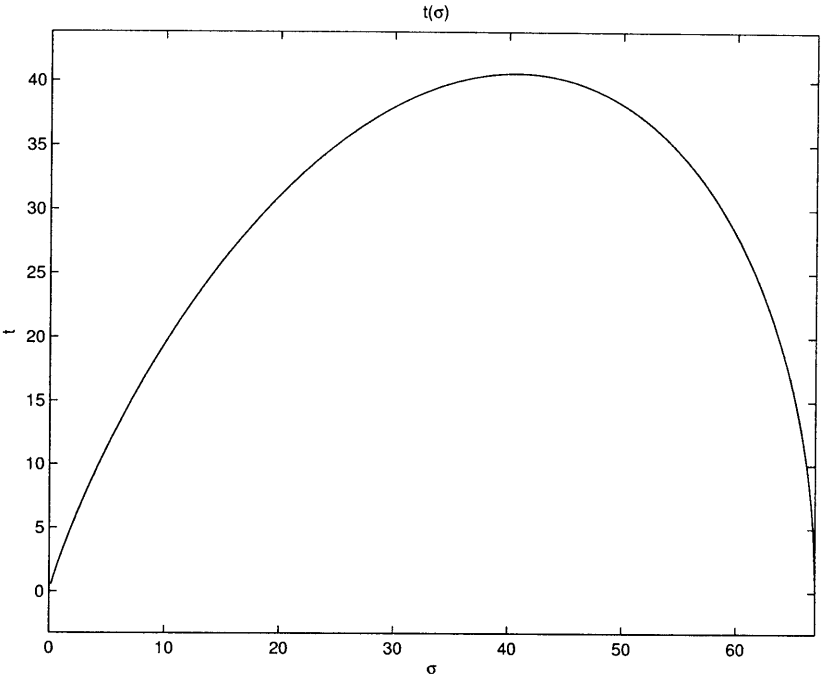

Figure 2-1: The curve of allowable (t, σ) values for given A and V, over the range $\sigma \in [0, \frac{A}{\sqrt{2\pi}V}]$.

the pulse width at $V = .561$. We can fix V and A, examine the allowable Gaussians which exist on a curve in $[\sigma, t]$ space, and then find σ where $t = \frac{PWT}{2}$.

Relevant equations include:

$$t = \sqrt{2\sigma^2 \ln \frac{A}{\sqrt{2\pi}V\sigma}} \tag{2.3}$$

$$\frac{dt}{d\sigma} = \sqrt{2 \ln \frac{A}{\sqrt{2\pi}V\sigma}} - \frac{1}{\sqrt{2 \ln \frac{A}{\sqrt{2\pi}V\sigma}}} \tag{2.4}$$

$$\frac{d^2t}{d\sigma^2} = \frac{-1}{\sqrt{2\sigma^2 \ln \frac{A}{\sqrt{2\pi}V\sigma}}} \left(1 + \frac{1}{2 \ln \frac{A}{\sqrt{2\pi}V\sigma}}\right) \tag{2.5}$$

These equations describe a Gaussian with a given total area, A, and a pulse width at threshold. The graph of $t(\sigma)$ is shown in fig. 2-1. As t and σ approach 0, the Gaussian approaches $A\delta(t)$, the Dirac delta function multiplied by A. At the other end of the graph, $t = 0$ and $\sigma = \frac{A}{\sqrt{2\pi}V}$, creating a wide Gaussian which only

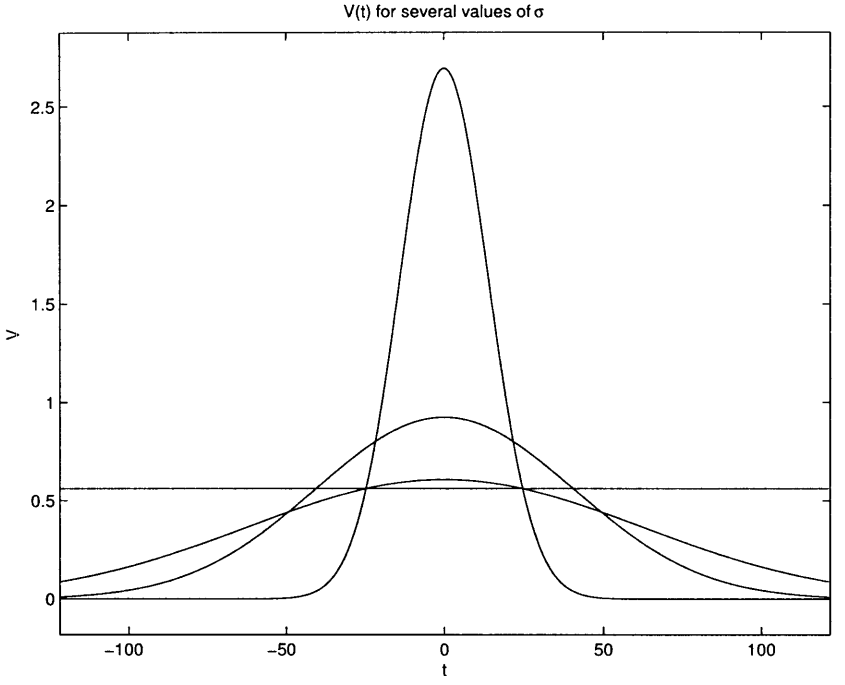

Figure 2-2: Three Gaussians plotted against the threshold voltage. Two different σ values are possible for a given pulse width at threshold. Two Gaussians cross the threshold at $t = \pm\frac{PWT}{2}$, one with $\sigma < t$ and one with $\sigma > t$. The third Gaussian has the pulse width equal to σ.

touches the threshold at $t = 0$. By setting $\frac{dt}{d\sigma} = 0$ and using eq. 2.3, we can see that $\sigma^* = \frac{A}{V\sqrt{2\pi e}} = t(\sigma^*)$, describing a Gaussian which crosses the threshold at its inflection points. For any value of $t < t(\sigma^*)$, there are two allowable values of σ. The larger σ value describes a broad Gaussian, while the smaller one describes a narrow Gaussian. See fig. 2-2. We are only interested in the values of σ below σ^*.

An iterated Taylor approximation of the pulse shape was performed, initially centered around $\sigma_0 = \frac{PWT}{2}$, half the pulsewidth at threshold. This is a good initial selection because different returns will occur at different points along the curve in fig. 2-1. Over the range $\sigma \in [0, \sigma^*]$ the curve is approximated by $t = \sigma$, to first order. We are trying to solve for σ at a given t, so the approximation begins with the very rough approximation that $\sigma_0 = t = \frac{PWT}{2}$. A quadratic Taylor approximation was made and then solved to find a better estimate of σ, which then became the center of a second approximation. This process was repeated until the difference between successive

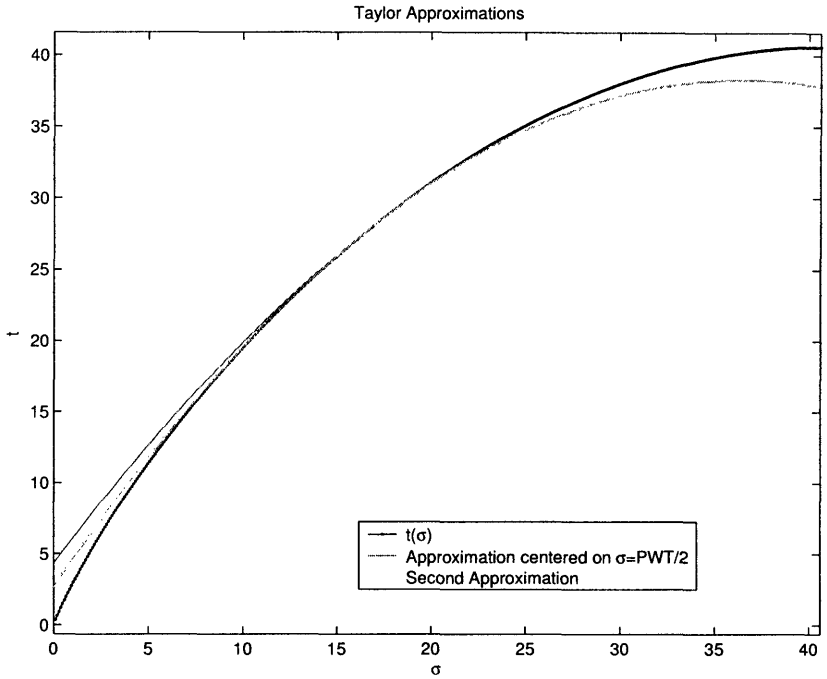

Figure 2-3: A plot showing the function t(σ) and its first and second approximations over the range [0,σ_{max}]. The data used is a typical MOLA return. The intersection of its second approximation and the threshold value agrees with more complex numerical calculations to better than four decimal places.

calculated σ values was below an ϵ, set here to .0001. These iterated approximations gave a very close fit, as can be seen in fig. 2-3. With this approximation, we can easily solve for σ given PWT, V, and the value of A calculated from eq. 2.1.

2.2 Comparison with Inversion Method

The Taylor approximation method uses energies calculated by the link equation, eq. 2.1. Abshire's method used energy measured directly by MOLA. Where the measured pulses are unsaturated, the two should agree. When the link equation uses the albedo measured actively by MOLA, there is close agreement, as seen in fig. 2-4. Due to the limitations of the MOLA instrumentation, the directly-measured energy is capped. The advantage of the Taylor approximation method is that it can provide roughness measurements beyond this saturation value.

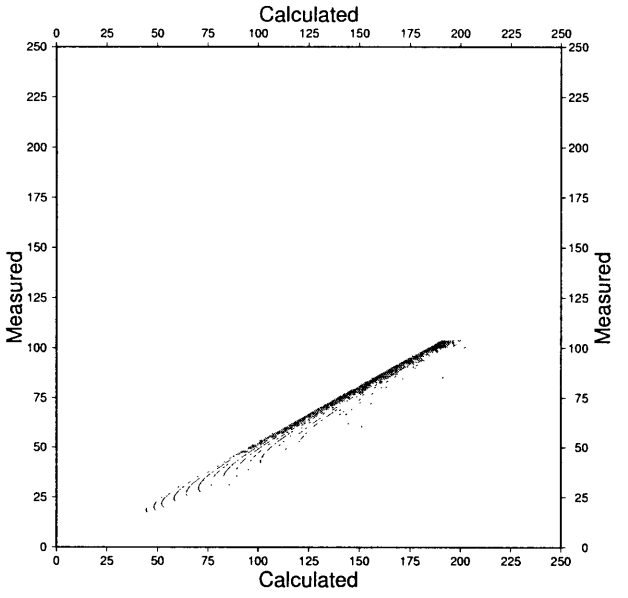

Figure 2-4: Energy measured for Abshire method vs energy calculated for the Taylor approximation method. Units are 10^{-15} J.

The close fit between the measured and calculated energy does not hold with other albedo measurements. Both the passive radiometry measurements and the HST measurements fail to show a linear relationship, as seen in fig. 2-5. Closer examination shows that this is due to a discrepancy in albedo in certain regions of the planet. Some regions have albedo measurements which result in agreement between calculated and measured energies. Other regions, such as Tharsis and Hellas, do not. However, pulsewidth is not correlated directly with energy (which is related to albedo through eq. 2.1).

This method of evaluationg σ by Taylor approximations was meant to provide a means of estimating surface roughness for regions of Mars over which Abshire's method fails. The Taylor approximation method should match up with the Abshire method over all regions where the Abshire method worked at all. Even though the calculated energies do not match up well, the calculated values of σ show some agreement with all measures of albedo. Using the MOLA-measured albedo shows good agreement for low values of σ. The divergence at high σ occurs because energy measurements in the Abshire method are capped while pulsewidths are not. Eq. 1.2

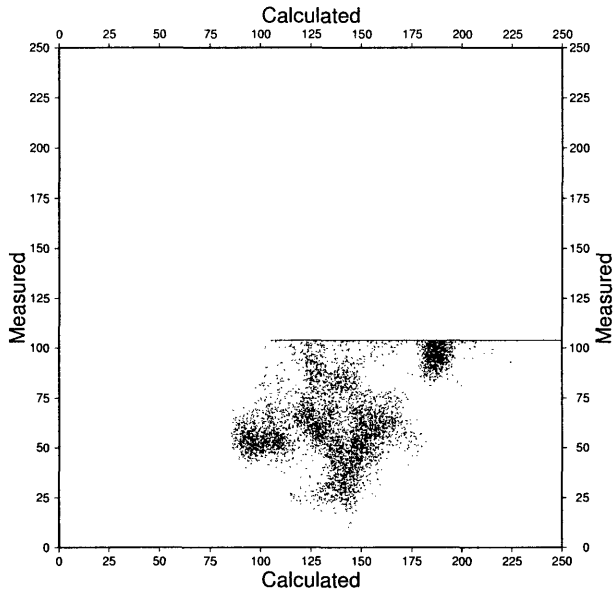

Figure 2-5: Energy measured for Abshire method vs energy calculated for the Taylor approximation method, using albedo averaged among all measurements. Units are 10^{-15} J.

shows that σ grows with increasing pulsewidth. See fig. 2-6.

As expected, given the poor comparison of energies, the σ values agree less well when the other albedo measurements are used. However, there is better agreement on σ, due to the weak dependence on A_y from eq. 1.2. Fig. 2-7 shows the same divergence at large values of σ, and only moderate agreement at low values.

2.3 Limitations

There are several instances in which a Gaussian approximation fails. Here, the measured pulsewidth at threshold is greater than the t^* of fig. 2-1. A Gaussian cannot be created that has the given integrated area and passes through the points defined by the pulsewidth and voltage threshold. The quadratic approximation then produces complex values of σ, which are clearly unphysical.

To get around this problem, energies calculated through the laser link equation were multiplied by a scale factor of 2. This removes some of the errors associated

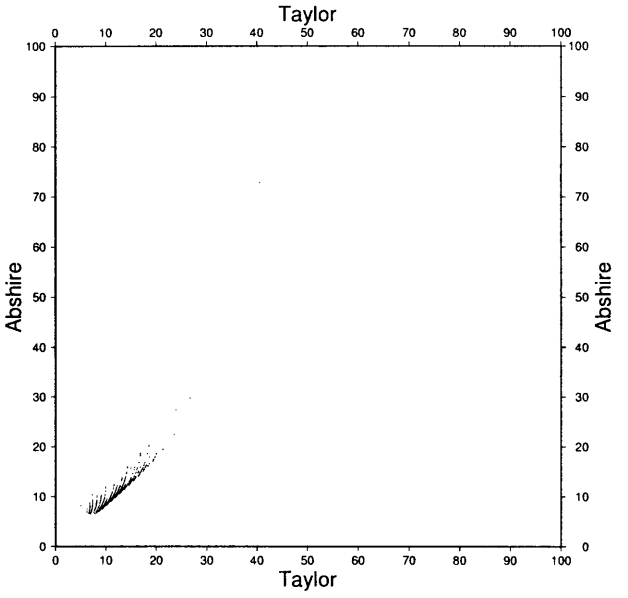

Figure 2-6: σ values calculated by the Taylor approximation method and by Abshire method, using MOLA albedo. Units are ns.

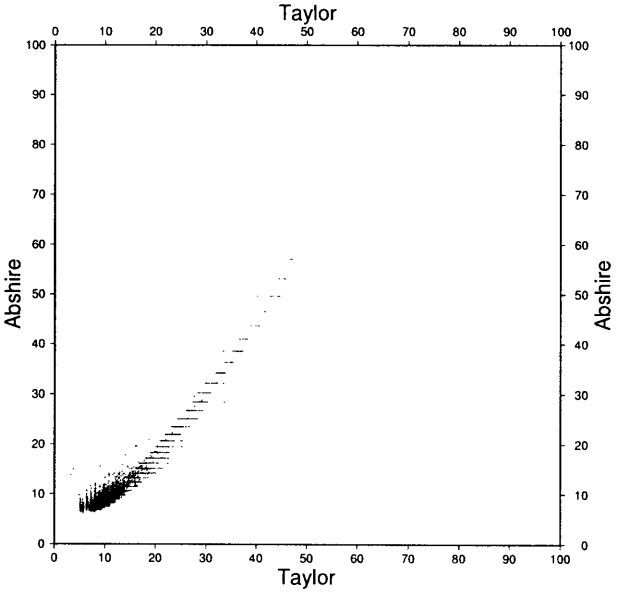

Figure 2-7: σ values calculated by the Taylor approximation method and by Abshire method, using averaged albedo values. Units are ns.

with the albedo measurements mentioned in chapter 1.

The failures occur when the calculated energy is too low to support broad pulses. In general, these failures will occur when the terrain is both rough (causing wider pulses) and of low albedo (and thus with lower returned energy). The failure rate remains low, less than one out of every thousand pulses.

Failures are not distributed uniformly around the planet. They are concentrated in a band reaching from 30°S to 45°S, with a few others scattered elsewhere. This distribution is unexpected. These anomalous points are not merely a result of polar ice reaching farther north than expected, in which case the failures would continue extending south.

Chapter 3

Surface Roughness Measurements

By applying the methods of the previous chapter to the MOLA data we can get an estimate of the surface roughness of Mars. These measurements were only made at latitudes between 50°N and 50°S. The north and south polar regions experienced seasonal albedo variations as ice caps grew and receded, making the data unreliable.

One calculation used an albedo averaged from the various measurements (fig. 3-1). A separate calculation was performed using the albedo measured actively by MOLA, using the same color scale (fig. 3-2).

For comparison (fig. 3-3), a map calculated using Abshire's method at the same resolution and with the same color scale. It is clear from the map that many areas of interest on the Martian surface simply cannot be measured using this technique. This map only plots unsaturated points. Certain regions, such as Tharsis, had many saturated returns. Therefore most of the data from these regions is not incorporated into the map. An examination of the map shows that σ values are generally lower here than they are on the other two maps. Fig. 2-6 shows that at high σ values, the Abshire calculation is larger than the Taylor approximation calculation. The lower σ values in the Abshire calculation may be a relic of the scale factor used to correct for albedo measurements, as mentioned in section 2.3.

The two different albedo values produce similar maps. The map using only MOLA-measured albedo has more sharply defined boundaries between smooth regions and rough ones than the averaged albedo map. This agrees with the earlier results on σ

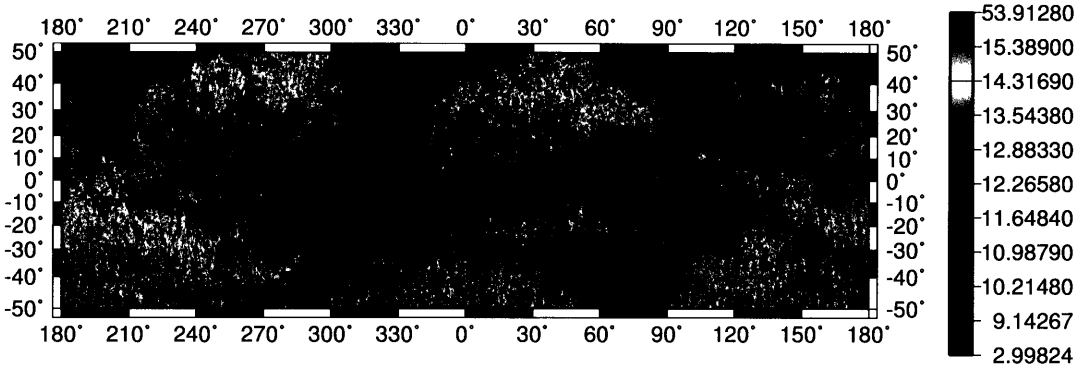

Figure 3-1: σ calculations over the Martian surface, using averaged albedo.

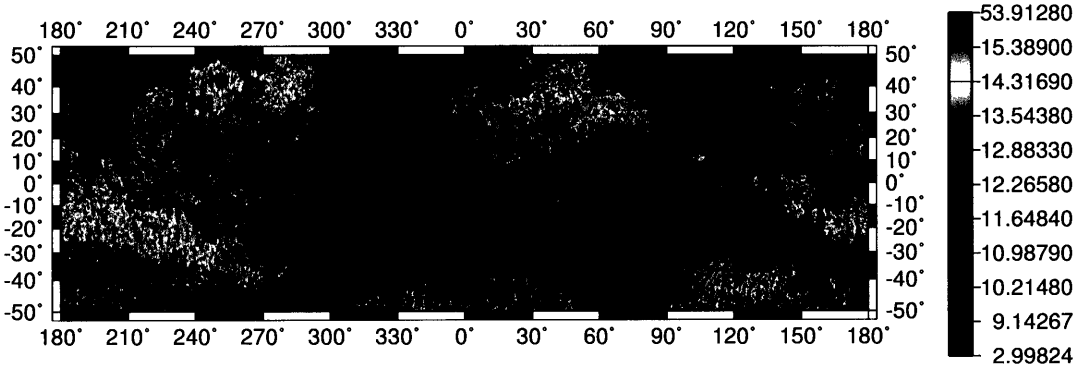

Figure 3-2: σ calculations over the Martian surface, using active MOLA albedo measurements.

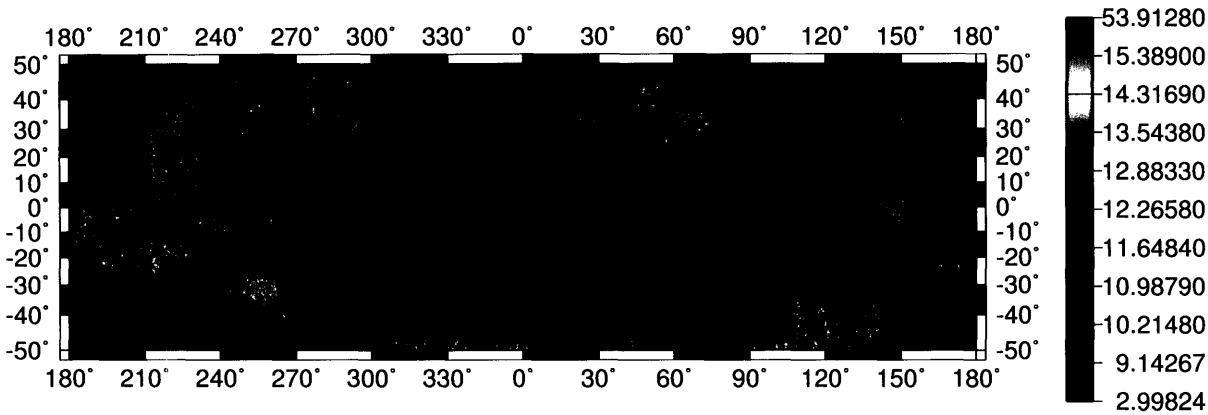

Figure 3-3: σ calculations over the Martian surface, using Abshire's method.

calculations for the different albedos, as in fig. 2-7. The averaged albedo tends to cause the calculated σ values to smear.

3.1 Regions of the Surface

3.1.1 Valles Marineris

Roughness measurements using this method fail around Valles Marineris. Due to sharp canyon walls, the laser returns did not trigger the first channel, and so were not included in these calculations.

3.1.2 Tharsis

As expected, the Tharsis region is one of the rougher regions of Mars. This area, extending from around 220°E to 300°E and from 0°N to 50°N, consists of volcanic, mountainous, and fractured terrain. The aureole of Olympus Mons, on the western edge of the Tharsis region, is an especially rough area. As can be seen in fig. 3-3, these rough regions had frequently saturated pulse returns. The individual peaks on Tharsis can be easily identified, and are rougher than the surrounding terrain.

In the analysis of fig. 2-5 it was mentioned that calculated energy matched measured energy for certain regions but that the two values did not agree for other regions. Tharsis is one region for which agreement is poor. Energies calculated from the link equation are higher than the energies measured by MOLA, saturation notwithstanding. The calculations of roughness here therefore represent an important test for the new method.

3.1.3 Hellas and Argyre

The Hellas impact basin, located from 35°E to 90°E and 30°S to 45°S is another region for which the calculated energy does not agree with measured energy in fig. 2-5. Due to cloud coverage, many pulses from this area did not trigger the first channel. As mentioned in chapter 1, this paper only used returns from this channel. Figures 3-1 and 3-2 show a lack of calculated σ values there. Additionally, the calculated σ values within Hellas are small, indicating that Hellas is one of the smoothest large areas on Mars. This does not agree with previous studies [9].

Hellas has an additional problem from atmospheric distortion. Due to the great depth of the crater, the atmospheric column is large and so there is often some attenuation of the laser pulses [10]. The methods used in this paper have ignored atmospheric effects, as they are small for much of the planet. They do become significant in some areas, such as Hellas, which have thicker atmospheres and frequent dust and cloud coverage.

The Argyre basin, located between 300°E and 330°E, and 40°S and 50°S, is barely visible on the two maps made in this paper. The region between the two basins is also smeared out and lacking the definition shown elsewhere on the two maps. Indeed, this region shows the highest concentration of failures in the σ calculations described in section 2.3. Failures are primarily located in a band around 40°S.

3.1.4 Syrtis Major

Syrtis Major (60°E to 90°E and 0°N to 20°N) is one of the darkest features on Mars. According to the calculated maps it is also one of the smoothest, along with Hellas. At the MOLA footprint length scale, this appears to be the smoothest region of the planet. Previous studies have noted the smoothness of Amazonis Planitia, just west and north of Tharsis, but at this length scale that region does not appear to be nearly as smooth as Syrtis Major or the Hellas basin [9].

Chapter 4

Conclusions

4.1 Overview

As shown in fig. 2-6, the calculated σ values for both the new method and the old agree for small values of σ while diverging at higher values. However, there are fewer values of σ at these higher values. These tend to be clustered geographically in a few regions, including Tharsis.

Saturated energy values lead to the calculation of incorrect σ values for roughness. However, for most laser returns these errors are not very large.

Because this method calculates pulse spreading from the returned energy, which is calculated through the link equation, eq 2.1, its accuracy is limited by albedo measurements. As mentioned in section 2.2, different albedo measurements do not always agree. The dependence of pulse spreading on returned energy is weak, and therefore reasonable estimates can be made with current albedo measurements. However, the differences between fig. 3-1 and 3-2 show that different albedos do lead to observable differences in calculated pulse widths.

4.2 Correcting for Dust Opacity

Martian weather is dominated by the dust storms which frequently globally encircle the planet. The omnipresent dust leads to distortions in measuring surface roughness.

This dust is about one micron in size, and so is comparable to the laser wavelength. The dust particles in the atmosphere reflect some light which further broadens the pulse width. A correction should be made so as to separate the spreading caused by atmospheric distortions from the spreading caused by surface scattering.

This analysis has not yet been performed, as data is lacking on the opacity of the dust at 1 micron. As this data becomes available it may become possible to connect dust absorption to MOLA pulses and thereby further improve the estimation of the atmospheric distortions on pulse spreading.

Bibliography

[1] D. E. Smith et al. Mars Orbiter Laser Altimeter: Experiment summary after the first year of global mapping of Mars. *J. Geophys. Res.*, 106:23,689–23,722, 2001.

[2] R. S. Afzal. Mars Orbiter Laser Altimeter: Laser transmitter. *Appl. Opt.*, 33:3184–3188, 1994.

[3] M. P. Golombek et al. Selection of Mars Exploration Rover landing sites. *J. Geophys. Res.*, 108:8072–8119, 2003.

[4] M. A. Kreslavsky and J. W. Head. Kilometer-scale roughness of Mars: Results from MOLA data analysis. *J. Geophys. Res.*, 105:26,695–26,711, 2000.

[5] J. B. Garvin, J. J. Frawley, and J. B. Abshire. Vertical roughness of Mars from the Mars Orbiter Laser Altimeter. *Geophys. Res. Lett.*, 26:381–384, 1999.

[6] G. A. Neumann et al. Mars Orbiter Laser Altimeter pulse width measurements and footprint-scale roughness. *Geophys. Res. Lett.*, 30:1561–1564, 2003.

[7] J. B. Abshire, X. Sun, and R. S. Afzal. Mars Orbiter Laser Altimeter: Receiver model and performance analysis. *Applied Optics*, 39:2449–2460, 2000.

[8] J. F. Bell et al. Near-infrared imaging of Mars from HST: Surface reflectance, photometric properties and implications for MOLA data. *Icarus*, 138:25–35, 1999.

[9] O. Aharonson, M. T. Zuber, and D. H. Rothman. Statistics of Mars' topography from the Mars Orbiter Laser Altimeter: Slopes, correlations, and physical models. *J. Geophys. Res.*, 106:23,723–23,735, 2001.

[10] G. A. Neumann, D. E. Smith, and M. T. Zuber. Two Mars years of clouds detected by the Mars Orbiter Laser Altimeter. *J. Geophys. Res.*, 108:5023–5039, 2003.